

Spatiotemporal Slip Distributions Associated with the 2018-2019 Bungo Channel Long-Term Slow Slip Event Inverted from GNSS Data

Yukinari Seshimo (✉ y.seshimo@stu.kobe-u.ac.jp)

Department of Planetology, Graduate School of Science, Kobe University

Shoichi Yoshioka

Research Center for Urban Safety and Security, Kobe University

Research Article

Keywords: Long-term slow slip events (L-SSEs), Bungo Channel, GNSS, spatiotemporal slip pattern

Posted Date: July 28th, 2021

DOI: <https://doi.org/10.21203/rs.3.rs-739946/v1>

License:  This work is licensed under a Creative Commons Attribution 4.0 International License.

[Read Full License](#)

Version of Record: A version of this preprint was published at Scientific Reports on January 10th, 2022.
See the published version at <https://doi.org/10.1038/s41598-021-03982-6>.

1 Spatiotemporal slip distributions associated
2 with the 2018-2019 Bungo Channel long-
3 term slow slip event inverted from GNSS
4 data

5
6 Yukinari Seshimo^{1,*} and Shoichi Yoshioka^{2,1}
7

8 ¹Department of Planetology, Graduate School of Science, Kobe University, Rokkodai-
9 cho 1-1, Nada ward, Kobe 657-8501, Japan

10 ²Research Center for Urban Safety and Security, Kobe University, Rokkodai-cho 1-1,
11 Nada ward, Kobe 657-8501, Japan
12

13
14
15 *corresponding author
16

17
18 TEL: +81-80-2624-6982

19 FAX: +81-78-803-6598

20 e-mail: y.seshimo@stu.kobe-u.ac.jp
21

22
23 Submitted to Scientific Reports on July 22, 2021
24
25
26

27 **Abstract**

28 Long-term slow slip events (L-SSEs) have occurred beneath the Bungo Channel with
29 durations of several months to a couple of years repeatedly with a recurrence interval of
30 approximately six years. We estimated the spatiotemporal slip distributions of the 2018-
31 2019 Bungo Channel L-SSE inverted from processed GNSS time series data. This event
32 was divided into two subevents, with the first on the southwest side of the Bungo Channel
33 from 2018.3 to 2018.7 and the second beneath the Bungo Channel from 2018.8 to 2019.4.
34 Tectonic tremors became active on the downdip side of the L-SSE occurrence region
35 when large slow slips took place beneath the Bungo Channel. Compared with the previous
36 Bungo Channel L-SSEs, this spatiotemporal slip pattern and amount were similar to those
37 of the 2003 L-SSE. However, the slip expanded in the northeast-southwest direction in
38 the latter half of the second subevent. We also found that the total duration of the two
39 subevents was 1.0 year, which was the shortest among the four recent L-SSEs beneath
40 the Bungo Channel identified using GNSS time series data. The maximum amount of slip,
41 the maximum slip velocity, the total released seismic moment, and the moment magnitude
42 of the 2018-2019 L-SSE were estimated to be 27 cm, 53 cm/year, 4.1×10^{19} Nm, and
43 7.0, respectively, all of which were the largest among the four L-SSEs.

44

45

46 **1. Introduction**

47 In the Bungo Channel, located between Shikoku and Kyushu in southwestern Japan,
48 the Philippine Sea plate is subducting beneath the Amurian plate in the northwest
49 direction at a convergence rate of approximately 58.4 ± 1.2 mm/year¹ (Fig. 1). On the
50 plate boundary beneath this region, aseismic interplate slips, which are so-called long-

51 term slow slip events (hereafter referred to as L-SSEs), have repeatedly occurred with
52 durations of several months to several years. The GNSS continuous observation system
53 (GEONET, GNSS Earth Observation Network System) launched by the Geospatial
54 Information Authority of Japan (GSI) in 1996 has enabled high-precision geodetic
55 observations with high temporal resolution and detection of such aseismic slow slip
56 events. GNSS observation stations have been set up at approximately 1,300 locations
57 throughout the Japanese Islands and play an important role in monitoring crustal
58 deformation caused by earthquakes and volcanic activities. Previous studies have
59 analysed the slip distributions of L-SSEs that occurred beneath the Bungo Channel in
60 1996-1998²⁻⁷, 2002-2004^{4, 6-8}, and 2009-2011⁷. Kobayashi and Yamamoto (2011)⁹
61 showed that L-SSEs also occurred in 1980, 1985-1986, and 1991 beneath the Bungo
62 Channel based on levelling survey and tide gauge station data and that the L-SSEs have
63 been repeated every 5-6 years since 1980.

64 Yoshioka et al. (2015)⁷ performed inversion analysis of the Bungo Channel L-SSEs
65 that occurred in 1996-1998, 2002-2004, and 2009-2011 and compared their
66 spatiotemporal slip distributions. In the 1996-1998 events, the maximum slip amount was
67 approximately 15 cm with Mw 6.8 and it was estimated that slip occurred beneath the
68 Ashizuri cape on the east side of the Bungo Channel from 1996.9. The slip area then
69 shifted to the central part of the Bungo Channel. The maximum slip amount of the 2002-
70 2004 event was estimated to be approximately 21 cm with Mw 7.0. The L-SSE during
71 this period consisted of two main subevents. The first subevent occurred on the southwest
72 side of the Bungo Channel from approximately 2002.1 to 2002.8 with the maximum slip
73 amount estimated to be approximately 7.3 cm with Mw 6.5. The second subevent
74 occurred from approximately 2003.1 to 2004.3 with the maximum slip amount estimated

75 to be approximately 16 cm with Mw 6.8. Furthermore, the second subevent can be divided
76 into three periods: 2003.1-2003.4, 2003.5-2004.0, and 2004.0-2004.3. The first slip
77 occurred in the southwest to central part of the Bungo Channel. The second slip started at
78 the northeast side of the Bungo Channel and expanded to the southwest with the
79 acceleration of the slip. The third slip was observed on the southwest side of the Bungo
80 Channel. In the 2009-2011 event, the maximum slip amount was approximately 19 cm,
81 Mw 6.9, and it was estimated that the slip started at approximately 2009.9 in the central
82 part of the Bungo Channel and then shifted to the southwest of the channel.

83 Ozawa et al. (2020)¹⁰ analysed the spatiotemporal slip distribution of the Bungo
84 Channel L-SSE that occurred from 2018 to 2019. They found that slip took place at the
85 plate boundary north of Hyuga-nada from June 2018 to October 2018 and at the Bungo
86 Channel from October 2018 to approximately August 2019. The maximum slip amount
87 was estimated to be approximately 30 cm beneath the Bungo Channel and 36 cm in
88 northern Hyuga-nada with Mw 7.0.

89 In this study, we used the inversion method proposed by Yoshioka et al. (2015)⁷ to
90 analyse the Bungo Channel L-SSE that occurred from 2018 to 2019 and compared the
91 results with spatiotemporal slip distributions of the previous Bungo Channel L-SSEs.

92

93

94 **2. Data processing of GNSS time series**

95 In this study, we used the daily coordinate positioning values (F3 solutions) of
96 GEONET stations provided by the Geospatial Information Authority of Japan. The data
97 period used for analysis covered 1 January 2016 to 30 June 2020. The number of
98 observation stations used was 114 (Fig. 1) with three components at each station. Six

99 stations (0075, 0076, 0385, 0387, 0388, and 0407) in the northern Chugoku district (Fig.
 100 1), which are not affected by the L-SSE, were used as reference stations to calculate the
 101 common-mode error. The analysis procedure was summarized as follows, according to
 102 Yoshioka et al. (2015)⁷. First, we calculated the residual,

$$103 \quad \varepsilon_i^S(d) = P_i^S(d) - C_i^S(d) \quad (1)$$

104 where $\varepsilon_i^S(d)$ is the residual, $P_i^S(d)$ is the time series data of the reference station after
 105 removing the coseismic steps and the steps caused by antenna exchange, $C_i^S(d)$ is the
 106 linear trend of the time series data of the reference station, and i ($= 1, 2,$ and 3) denote
 107 the east-west, north-south, and up-down components, respectively. Next, the residuals of
 108 the six stations were averaged to obtain the common-mode error:

$$109 \quad \hat{\varepsilon}_i(d) = \frac{1}{6} \sum_{s=1}^6 \varepsilon_i^S(d) \quad (2)$$

110 Assuming that this error component is common to all the stations used in the analysis, we
 111 removed the common-mode error from the time series data of each station.

$$112 \quad \hat{O}_i^T(d) = O_i^T(d) - \hat{\varepsilon}_i(d) \quad (3)$$

113 where $O_i^T(d)$ denotes the original time series data of each observation station. After
 114 removing the common-mode error, we calculated the crustal movement due to plate
 115 motions and annual and semiannual variations and removed these components.

$$116 \quad y(t) = a + bt + \sin\left(\frac{2\pi t}{T}\right) + d \cos\left(\frac{2\pi t}{T}\right) + e \sin\left(\frac{4\pi t}{T}\right) + f \cos\left(\frac{4\pi t}{T}\right) \quad (4)$$

117 where $T = 1$ year, the first and second terms on the right-hand side represent crustal
 118 deformation due to plate motions assuming a linear trend, the third and fourth terms
 119 represent annual variations, and the fifth and sixth terms represent semiannual variations.

120 a to f are unknown parameters and their optimal values were determined by the least-
 121 squares method. The period used for the calculation of equation (4) was from 1 January

122 2016 to 31 December 2017, when no L-SSEs took place, and these components were
123 assumed to be invariant during the entire analysis period. After removing the coseismic
124 steps and the steps caused by antenna exchange, we also removed the crustal deformation
125 caused by plate motion, annual variations and semiannual variations. The coseismic steps
126 and the steps caused by the antenna exchange were corrected by taking the difference of
127 the average of the previous and next 10 days. The corrected time series data were
128 subjected to curve fitting using a cubic B-spline function using ABIC (Akaike's Bayesian
129 Information Criterion) minimization principle¹¹ to estimate the standard deviation of the
130 data used for the inversion of the spatiotemporal slip distribution of L-SSE. In addition,
131 the corrected time series data show larger variations in the vertical displacements than
132 those in the horizontal displacements.

133

134

135 **3. Model**

136 Since the L-SSE is a slip phenomenon occurring on the plate boundary, the
137 estimation area is placed on the three-dimensional upper surface of the Philippine Sea
138 plate, as shown in Hirose et al. (2008)¹² (Fig. 1). The size of the source region at the plate
139 interface was 200 km × 200 km in the dip and strike directions, respectively, and 11 × 11
140 B-spline functions were distributed as the basis functions. The number of basis functions
141 in the time direction was 21. Therefore, the total number of model parameters
142 representing the spatiotemporal slip distribution was 5082, where the slip was represented
143 by two components, the dip and strike directions. The means of the standard deviations
144 used to weight the EW, NS, and UD components during inversion were 0.14 cm, 0.14 cm,
145 and 0.52 cm, respectively, which were obtained using the optimal curve and daily

146 corrected positioning time series data, as described in the previous section. In this study,
147 the time step was set to 0.1 year.

148

149

150 **4. Results**

151 **4-1. Horizontal and vertical displacement rates associated with the L-SSE**

152 The total horizontal and vertical displacements associated with the L-SSE at each
153 station during the analysis period are shown in Figs. S1 (a) and (b), respectively. In the
154 horizontal displacement field, a maximum displacement of approximately 5 cm in the
155 southeast and east-southeast directions was identified at most stations. In the vertical
156 displacement field, a maximum subsidence of approximately 5 cm was identified in
157 eastern Kyushu, and a maximum uplift of approximately 5.5 cm was observed in
158 southwestern Shikoku.

159 The corrected time series three-component data at some picked-up stations in Fig.
160 S1(a) are shown in Fig. S2. At the stations in Kyushu, southeastward displacements
161 associated with the 2018-2019 Bungo Channel L-SSE began to be observed from the
162 middle of 2018 and subsided in the middle of 2019. The maximum displacements were
163 approximately 1.5 cm in the south direction, approximately 2.9 cm in the east direction,
164 and approximately 2.8 cm in the downward direction among the stations in Kyushu, as
165 shown in Fig. S2. The southeastward displacements also began to be observed at stations
166 in Shikoku in the middle of 2018 and subsided in the middle of 2019. The time when the
167 displacements subsided was almost the same as that in Kyushu. The maximum
168 displacements were approximately 2.6 cm in the south direction, approximately 3.4 cm
169 in the east direction, and approximately 4.6 cm in the upward direction among the stations

170 in Shikoku, as shown in Fig. S2. In particular, the uplift at the station located in the
171 southwestern part of Shikoku was approximately 2 to 3 cm larger than that at other
172 stations in Shikoku.

173 Horizontal displacements at 0.1-year time steps are shown in Fig. 2. Displacement
174 rates in the southeast to east-southeast directions began to be observed at both stations in
175 Kyushu and Shikoku in approximately 2018.4 (Fig. 2(e)). During the period from 2018.5
176 to 2018.6 (Fig. 2(f)), the displacement rates became larger. The increase in displacement
177 was especially pronounced at the stations in Kyushu, where the maximum displacement
178 rate was approximately 5 cm/year. During the period from 2018.6 to 2018.7 (Fig. 2(g)),
179 the displacement rates decreased, and during the period from 2018.7 to 2018.8 (Fig. 2(h)),
180 almost no displacement was observed. Subsequently, the displacement rates in the east-
181 southeast direction appeared during the period from 2018.8 to 2018.9 (Fig. 2(i)). The
182 displacement rates became the largest during the period from 2019.1 to 2019.2 (Fig. 2(l)),
183 with a maximum displacement rate of approximately 11 cm/year. After that, the
184 displacement rates decreased, and almost no displacement was observed during the period
185 from 2019.4 to 2019.5 (Fig. 2(o)). In contrast to the displacement rates observed during
186 the period from 2018.3 to 2018.7 (Fig. 2(d)-(g)), during the period from 2018.8 to 2019.4
187 (Fig. 2(i)-(n)), displacement rates in the southeast to east-southeast direction were
188 observed mainly at stations in the northern part of Kyushu, reaching approximately 7
189 cm/year, and the displacement rates at stations in the southwestern part of Shikoku
190 became larger by approximately 8 cm/year. After southeast to east-southeast displacement
191 rates were observed in both Kyushu and Shikoku during the period from 2018.8 to 2019.4
192 (Fig. 2(i)-(n)), east-southeastward displacement rates up to approximately 3 cm/year were
193 observed mainly in Shikoku during the period from 2019.5 to 2019.6 (Fig. 2(p)).

194 The vertical displacement at 0.1-year time steps is shown in Fig. 3. Uplift began
195 gradually in the southwestern part of Shikoku in approximately 2018.9 (Fig. 3(j)) and
196 became the largest during the period from 2019.1 to 2019.3 (Fig. 3(l)-(m)), reaching
197 approximately 14 cm/year. After that, the displacement rates decreased. Subsidence,
198 reaching approximately 5 cm/year, can be identified at most of the stations in Kyushu
199 during the period from 2019.0 to 2019.1 (Fig. 3(k)).

200

201 **4-2. Spatiotemporal slip distributions associated with the L-SSE inverted from** 202 **the GNSS data**

203 The inversion analysis of the spatiotemporal slip distribution on the 3-D shaped
204 plate boundary was performed from 2018.0 to 2020.0 using the corrected time series
205 GNSS data of each observation station. The spatiotemporal slip distributions inverted
206 from the horizontal displacement (Fig. 2) and vertical displacement (Fig. 3) data at 0.1-
207 year time steps are shown in Fig. 4. The maximum amount of slip, released seismic
208 moment, and equivalent moment magnitude were estimated to be approximately 27 cm,
209 4.1×10^{19} Nm, and 7.0, respectively (Table S1). The rigidity used in the calculation of
210 seismic moments was 30 GPa. Here, we evaluated the minimum released seismic moment
211 and equivalent M_w , although the seismic moment appears to increase even after the
212 second subevent (Figs. S3). This point will be discussed later.

213 The L-SSE that occurred during this period consists of two subevents. The first
214 subevent was identified on the southwest side of the Bungo Channel during the period
215 from 2018.3 to 2018.7 (Figs. 4 (d)-(g)). The maximum amount of slip, released seismic
216 moment, and equivalent moment magnitude were estimated to be approximately 8.2 cm,

217 9.0×10^{18} Nm, and 6.6, respectively. The maximum slip velocity was approximately 36
218 cm/year during the period from 2018.5 to 2018.6 (Fig. 4(f)).

219 The second subevent was identified beneath the central Bungo Channel area during
220 the period from 2018.8 to 2019.4 (Figs. 4 (i)-(n)). The maximum amount of slip, released
221 seismic moment, and equivalent moment magnitude were estimated to be approximately
222 19 cm, 2.2×10^{19} Nm, and 6.8, respectively. The maximum slip velocity was
223 approximately 53 cm/year during the period from 2019.1 to 2019.2 (Fig. 4(l)). In this
224 subevent, the slip area expanded in the northeast-southwest direction during the period
225 from 2019.2 to 2019.3 (Fig. 4(m)). In addition, tectonic tremors appear to have been
226 activated on the downdip side of the L-SSE occurrence region when large slips occurred
227 beneath the Bungo Channel. After the end of the second subevent, a slight slip appears to
228 take place during the period from 2019.4 to 2019.8 (Figs. 4 (o)-(r) and S3).

229 Here, we compare the calculated values obtained from the slip distributions shown
230 in Fig. 4 with the observed values. In Fig. 2, the directions of the observed and calculated
231 horizontal displacement rates were almost the same at most stations, although the
232 calculated values were more east-southeast than the observed values at some stations. The
233 displacement rates were almost the same, although the calculated values were smaller
234 than the observed values at some stations. During the period from 2019.5 to 2019.7, the
235 observed displacement rates were not clearly identified, but the calculation showed
236 displacement rates from east-southeast to southeast in the southwestern part of Shikoku.

237 In Fig. 3, we show a comparison between the observed and calculated vertical
238 displacement fields. Agreement in these data is not as good as that of the horizontal
239 displacement fields because the data weight for the latter is larger than that for the former.
240 There was a large difference between the observed and calculated displacement rates at

241 the stations in Kyushu, but the difference was relatively small at the stations in Shikoku.
242 In particular, the observed and calculated values were almost identical during the period
243 from 2019.1 to 2019.3 (Figs. 3(l) and (m)), when the southwestern part of Shikoku was
244 greatly uplifted.

245 A similar tendency can also be identified from the time series data at some picked-
246 up stations (Fig. S2). The fitting of the calculation to the corrected horizontal time series
247 data is better than that of the vertical data, and the discrepancy tends to be slightly larger
248 in the vertical component at the stations in Kyushu.

249

250

251 **5. Discussion**

252 **5-1. Comparison with spatiotemporal slip distributions of the past L-SSEs beneath** 253 **the Bungo Channel**

254 L-SSEs occurred beneath the Bungo Channel in the past. Here, based on the results
255 obtained by Yoshioka et al. (2015)⁷, we compared the characteristics of slips of the L-
256 SSEs that occurred in 1996-1998, 2002-2004, and 2009-2011 with that of the L-SSE
257 estimated in this study (Table S1). The first subevent of the L-SSE estimated in this study
258 occurred on the southwest side of the Bungo Channel and the second subevent took place
259 beneath the central part of the Bungo Channel. The location, magnitude, spatial slip
260 distribution, and relative order in time and space in 2018-2019 were all similar to those
261 of the 2002-2004 L-SSE (Fig. S4).

262 However, the time interval between the first and second subevents was 0.3 years in
263 the 2002-2004 L-SSE, while it was 0.1 years in the 2018-2019 L-SSE and the slip area
264 expanded in the northeast-southwest direction in the latter half of the second subevent

265 (Figs. 4 (m) and (n)) in the 2018-2019 L-SSE. We also found that the total duration time
266 of the two subevents was 1.0 year, which was the shortest among the four recent L-SSEs
267 beneath the Bungo Channel identified using GNSS time series data.

268 The time variation of the cumulative released seismic moment of the 2018-2019
269 L-SSE is shown in Fig. S3. The released seismic moment and equivalent moment
270 magnitude of the first and second subevents of the L-SSE estimated in this study were
271 almost the same as those of the first and second subevents of the 2002-2004 L-SSE. In
272 addition, the released seismic moment and equivalent moment magnitude of the second
273 subevent estimated in this study were almost the same as those of the 1996-1998 and
274 2009-2011 L-SSEs. The duration of the slip was approximately 1.3 years for the 1996-
275 1998 L-SSE, approximately 0.7 years for the first subevent, approximately 1.2 years for
276 the second subevent of the 2002-2004 L-SSE, and approximately 1.2 years for the 2009-
277 2011 L-SSE. On the other hand, the durations of the first and second subevents of the
278 2018-2019 L-SSE were approximately 0.4 and 0.6 years, respectively. Thus, the total
279 duration of slips was the shortest for the 2018-2019 L-SSE among the four L-SSEs. In
280 the 1996-1998 L-SSE, 2002-2004 L-SSE, 2009-2011 L-SSE, and 2018-2019 L-SSE, the
281 maximum slip velocity was approximately 28 cm/year, 44 cm/year, 39 cm/year, and 53
282 cm/year, respectively, and the total slip was approximately 15 cm, 21 cm, 19 cm, and 27
283 cm, respectively. The maximum slip velocities, which also resulted from the shortest
284 duration, and the total slip of the L-SSEs estimated in this study were the largest among
285 the four L-SSEs beneath the Bungo Channel. The occurrence interval of L-SSEs in the
286 past was approximately six years, but the estimated L-SSE in this study was
287 approximately eight years after the last L-SSE in 2009-2011. This may have affected the
288 maximum slip rate and total slip.

289 Hirose et al. (2010)¹³ found that tectonic tremors and shallow very low-frequency
290 earthquakes located near the Nankai Trough far to the south were synchronized in the
291 2002-2004 L-SSE and the 2009-2011 L-SSE. In this study, an increase in tectonic tremors
292 was identified, but synchronization with shallow very low-frequency earthquakes has not
293 yet been investigated.

294

295 **5-2. Comparison with a previous study on spatiotemporal slip distributions of the** 296 **2018-2019 Bungo Channel L-SSE**

297 Next, we compared the spatiotemporal slip distributions of the 2018-2019 Bungo
298 Channel L-SSE obtained in this study with those obtained in a previous study. Ozawa et
299 al. (2020)¹⁰ performed a network filter inversion by McGuire and Segall (2003)¹⁴ and
300 found that the first subevent occurred on the north side of Hyuga-nada from June 2018 to
301 October 2018 and the second subevent was identified beneath the Bungo Channel from
302 October 2018 to August 2019. The locations of the two subevents were almost the same
303 as those obtained in this study. In Ozawa et al. (2020)¹⁰, the second subevent also
304 expanded in the northeast-southwest direction. The maximum amount of slip was
305 estimated to be approximately 30 cm by Ozawa et al. (2020)¹⁰, which was almost the
306 same as that estimated in this study. The moment magnitude of the L-SSE was estimated
307 to be 7.0, which was consistent with the results of this study.

308 However, there were also some discrepancies between the two studies. First, the
309 start time of the first subevent was different from that of this study. In addition, during
310 the period from 1 April 2019 to 1 June 2019, the slip near the centre of the Bungo Channel
311 weakened, and slip was identified on the southwest side of Shikoku and the north side of
312 Hyuga-nada in Ozawa et al. (2020)¹⁰, whereas there was no weakening of the slip near

313 the centre of the Bungo Channel in this study. Furthermore, the slip weakened in the
314 period from June 2019 to August 2019 in Ozawa et al. (2020)¹⁰, but in this study, a slight
315 slip was identified in the period from 2019.4 to 2019.8 (Figs. 4 (o)-(r)). This suggested
316 that the slip may have continued even after August 2019. Another possibility is that this
317 difference may originate from the fact that the postseismic deformations associated with
318 the 2011 Tohoku earthquake, especially eastward slight continuous displacements, as seen
319 in Fig. S3 (b), have not been completely removed in this study, in which a linear trend is
320 assumed and detrended, resulting in superficial slight slip in Figs. 4 (o)-(r).

321 These differences may be caused by differences in the temporal resolution of the
322 slip distributions, the difference in the correction of the GNSS time series data, and the
323 difference in the inversion method. With regard to the temporal resolution, Ozawa et al.
324 (2020)¹⁰ explained the temporal change in slip using the slip distribution every two
325 months, while in this study, we used the slip distribution every 0.1 year. In Ozawa et al.
326 (2020)¹⁰, the period of the time step was longer than that of this study, so the slip amount
327 at each time step was expected to be larger. For the correction of the GNSS time series
328 data, Ozawa et al. (2020)¹⁰ used the estimation period of the annual variations from 2000
329 to 2018 and the linear trend from 1 January 2017 to 1 January 2018, while in this study,
330 the estimation period of both the annual and semiannual variations and the linear trend
331 was from 1 January 2016 to 31 December 2017. For the inversion method, Ozawa et al.
332 (2020)¹⁰ used the constraints that the aseismic slip vector and slip vector at the plate
333 interface should be within 10° from the direction opposite to the relative motion of the
334 Philippine Sea plate to the Amurian plate and did not give any constraints in the time
335 direction, while in this study, we used the three prior constraints as described in the
336 “Methods” section.

337

338

339 **6. Conclusions**

340 In this study, we analysed the spatiotemporal slip distributions of the long-term
341 slow slip event that occurred on the plate boundary beneath the Bungo Channel from 2018
342 to 2019 using GNSS time series data. We used the inversion method proposed by
343 Yoshioka et al. (2015)⁷ with the three prior constraints. Significant results obtained in this
344 study can be summarized as follows:

345 (1) Regarding the 2018-2019 L-SSE analysed in this study, the total duration time of 1.0
346 year was the shortest, and the slip velocity of 53 cm/year, slip amount of 27 cm, total
347 amount of released seismic moment of 4.1×10^{19} Nm, and equivalent moment
348 magnitude of 7.0 were all the largest among the four L-SSEs which were recorded
349 by GNSS. The latter may be related to the longest recurrence interval of eight years
350 since the occurrence of the last L-SSE.

351 (2) The 2018-2019 L-SSE consists of two subevents. The first subevent occurred on the
352 southwest side of the Bungo Channel, with a maximum slip of approximately 8.2
353 cm, released seismic moment of 9.0×10^{18} Nm, equivalent M_w of 6.6, and
354 maximum slip velocity of approximately 36 cm/year during the period from 2018.5
355 to 2018.6. The second subevent took place near the centre of the Bungo Channel,
356 with a maximum slip of approximately 19 cm, a released seismic moment of
357 2.2×10^{19} Nm, an equivalent M_w of 6.8, and a maximum slip velocity of
358 approximately 53 cm/year during the period from 2019.1 to 2019.2.

359 (3) Tectonic tremors appear to have been activated on the downdip side of the L-SSE
360 occurrence region when large slips occurred beneath the Bungo Channel.

361 (4) Compared with the past L-SSEs beneath the Bungo Channel, the first subevent
362 occurred on the southwest side of the Bungo Channel and the second subevent took
363 place near the centre of the Bungo Channel, which is similar to the 2002-2004 L-
364 SSEs. The released seismic moment and equivalent M_w were almost the same.

365

366

367 **Methods**

368 We performed an inversion analysis for the crustal deformation associated with the
369 2018-2019 Bungo Channel L-SSE by the following procedure using corrected GNSS time
370 series data. The medium is assumed to be a semi-infinite homogeneous perfect elastic
371 body.

372 In this study, we used the inversion method proposed by Yoshioka et al. (2015)⁷
373 with three prior constraints: 1) the spatial slip distribution is smooth, 2) the slip directions
374 are oriented in the direction of plate convergence, and 3) the temporal change in the slip
375 is smooth. The slip distribution is represented by a superposition of bicubic B-spline
376 functions, and the temporal evolution is represented by a superposition of first-order B-
377 spline functions. In the following, we briefly summarize the inversion method according
378 to Yoshioka et al. (2015)⁷. The relationship between the model parameters representing
379 the spatiotemporal slip distribution and the observed data can be expressed by the
380 following equation:

$$\begin{bmatrix} \mathbf{d} \\ \mathbf{0} \\ \mathbf{0} \\ \mathbf{0} \end{bmatrix} = \begin{bmatrix} \mathbf{H} \\ \hat{\alpha}\mathbf{A} \\ \hat{\beta}\mathbf{B} \\ \hat{\gamma}\mathbf{G} \end{bmatrix} [\mathbf{a}] \quad (5)$$

381 where \mathbf{d} is the vector of observed displacement data, \mathbf{H} is a matrix representing the
382 relationship between the unit slip on the fault plane and the displacement at each GNSS

383 observation station, \mathbf{a} is a vector of model parameters, \mathbf{A} , \mathbf{B} , and \mathbf{G} are matrices
 384 representing the above-described first, second and third constraints, respectively. $\hat{\alpha}$, $\hat{\beta}$,
 385 and $\hat{\gamma}$ are the optimal values of the hyperparameters and represent the optimal values of
 386 the weight of the constraints. These hyperparameters are determined uniquely and
 387 objectively based on the ABIC minimization principle¹¹. A covariance matrix \mathbf{C} of the
 388 estimation error for the estimated model parameter vector can be obtained as follows:

$$389 \quad \mathbf{C} = \hat{\sigma}^2 (\mathbf{H}^T \mathbf{H} + \hat{\alpha}^2 \mathbf{A}^T \mathbf{A} + \hat{\beta}^2 \mathbf{B}^T \mathbf{B} + \hat{\gamma}^2 \mathbf{G}^T \mathbf{G})^{-1} \quad (6)$$

390 where $\hat{\sigma}^2$ is described in Yoshioka et al. (2015)⁷. A resolution matrix can be defined as

$$391 \quad \mathbf{R} = (\mathbf{H}^T \mathbf{H} + \hat{\alpha}^2 \mathbf{A}^T \mathbf{A} + \hat{\beta}^2 \mathbf{B}^T \mathbf{B} + \hat{\gamma}^2 \mathbf{G}^T \mathbf{G})^{-1} \mathbf{H}^T \mathbf{H} \quad (7)$$

392 The value of the resolution at each solved point on the plate boundary is defined by the
 393 diagonal component of the resolution matrix as

$$394 \quad R = \sqrt{\frac{(R^P)^2 + (R^S)^2}{2}} \quad (8)$$

395 where R^P and R^S are the resolutions in the plate convergence direction and
 396 perpendicular to the plate convergence direction, respectively.

397 In this study, we evaluated the reliability of the inverted slip distributions using the
 398 calculated estimation errors and resolutions.

399 The optimal values of the hyperparameters representing the weights of the three
 400 prior constraints $\hat{\alpha}$, $\hat{\beta}$, and $\hat{\gamma}$ used in this study were obtained as 7.4×10^{-2} , $6.7 \times$
 401 10^{-1} , and 7.4×10^{-2} , respectively.

402
 403

404 **Acknowledgements**

405 We thank T. Yabuki for sharing the source code of geodetic data inversion used in
 406 Yabuki and Matsu'ura (1992)¹⁵. We also thank Geospatial Information Authority of Japan
 407 and National Research Institute for Earth Science and Disaster Resilience for allowing us
 408 to use daily GNSS time series data (<https://terras.gsi.go.jp/>) and hypocenter catalogue of
 409 tectonic tremors (<https://hinetwww11.bosai.go.jp/auth/?LANG=ja>), respectively. Figures

410 were created by using the Generic Mapping Tools (GMT)¹⁶ (version: GMT 4.5.7, URL
411 link: <https://www.generic-mapping-tools.org/download/>). This work was partly supported
412 by Japan Society for the Promotion of Science grants KAKENHI 16H04040 and
413 16H06477. The part of this research is also supported by The Project for Hazard
414 Assessment of Large Earthquakes and Tsunamis in the Mexican Pacific Coast for Disaster
415 Mitigation, SATREPS funded by JST-JICA (#1554361).

416

417

418 **Author Contributions statement**

419 Y.S. carried out the data processing of GNSS time series and carried out the
420 inversion analyses, and wrote the paper; S.Y. organized and instructed this study, pointing
421 out possible problems and advised the solutions to those in this study. Both authors
422 reviewed and commented on the paper as well as declare no competing interests in
423 relation to the work.

424

References

Commented [Y1]:本文中に出てくる順に番号を着けて、参考文献を書く。

- 425 1. DeMets, C., Gordon, R. G. & Argus, D. F. Geologically current plate motions.
426 *Geophys. J. Int.* **181**, 1-80 (2010).
- 427 2. Hirose, H., Hirahara, K., Kimata, F., Fujii, N. & Miyazaki, S. A slow thrust slip event
428 following the two 1996 Hyuganada earthquakes beneath the Bungo Channel,
429 southwest Japan. *Geophys. Res. Lett.* **26**, 3237–3240 (1999).
- 430 3. Ozawa, S., Murakami, M. & Tada, T. Time-dependent inversion study of the slow
431 thrust event in the Nankai trough subduction zone, southwestern Japan. *J. Geophys.*
432 *Res.* **106**, 787–802 (2001).
- 433 4. Ozawa, S., Suito, H., Imakiire, T. & Murakami, M. Spatiotemporal evolution of
434 aseismic interpolate slip between 1996 and 1998 and between 2002 and 2004, in
435 Bungo channel, southwest Japan. *J. Geophys. Res.* **112**, B05409 (2007).
- 436 5. Miyazaki, S., McGuire J. J. & Segall, P. A transient subduction zone slip episode in
437 southwest Japan observed by the nationwide GPS array. *J. Geophys. Res.* **108**, B2,
438 2087 (2003).
- 439 6. Liu, Z. *et al.* Integration of transient strain event with models of plate coupling and
440 areas of great earthquakes in southwest Japan. *Geophys. J. Int.* **181**, 1292–1312
441 (2010).
- 442 7. Yoshioka, S., Matsuoka, Y. & Ide, S. Spatiotemporal slip distributions of three long-
443 term slow slip events beneath the Bungo Channel, southwest Japan, inferred from
444 inversion analyses of GPS data. *Geophys. J. Int.* **201**, 1437-1455 (2015).
- 445 8. Ozawa, S. *et al.* Aseismic slip and low-frequency earthquakes in the Bungo channel,
446 southwestern Japan. *Geophys. Res. Lett.* **31**, L07609 (2004).
- 447 9. Kobayashi, A. & Yamamoto, T. Repetitive long-term slow slip events beneath the
448 Bungo Channel, southwestern Japan, identified from leveling and sea level data from
449 1979 to 2008. *J. Geophys. Res.* **116**, B04406 (2011).
- 450 10. Ozawa, S., Kawabata, R., Kokado, K. & Yurai, H. Long-term slow slip events along
451 the Nankai trough delayed by the 2016 Kumamoto earthquake, Japan. *Earth, Planets*
452 *and Space.* **72**:61 (2020).
- 453 11. Akaike, H. Likelihood and Bayes procedure. in *Bayesian Statistic.* eds Bernardo,
454

- 455 J.M., DeGroot, M.H., Lindley, F.V. & Smith, A.F.M., University Press. 143-166
456 (1980).
- 457 12. Hirose, F., Nakajima, J. & Hasegawa, A. Three-dimensional seismic velocity
458 structure and configuration of the Philippine Sea slab in southwestern Japan
459 estimated by double-difference tomography. *J. Geophys. Res.* **113**, B09315 (2008).
- 460 13. Hirose, H. *et al.* Slow earthquakes linked along dip in the Nankai subduction zone.
461 *Science* **330**, 1502 (2010).
- 462 14. McGuire, J. J. & Segall, P. Imaging of aseismic slip transients recorded by dense
463 geodetic networks. *Geophys. J. Int.* **155**, 778–788 (2003).
- 464 15. Yabuki, T. & Matsu'ura, M. Geodetic data inversion using a Bayesian information
465 criterion for spatial distribution of fault slip. *Geophys. J. Int.* **109**, 363–375 (1992).
- 466 16. Wessel, P., & Smith, W.H.F. New, improved version of the generic mapping tools
467 released. *EOS Trans. AGU* **79**, 579 (1998).
- 468 17. Baba, T., Tanioka, Y., Cummins, P.R. & Uhira, K. The slip distribution of the 1946
469 Nankai earthquake estimated from tsunami inversion using a new plate model. *Phys.*
470 *Earth planet. Inter.* **132**, 59–73 (2002).
- 471 18. Nakajima, J. & Hasegawa, A. Subduction of the Philippine Sea plate beneath
472 southwestern Japan: Slab geometry and its relationship to arc magmatism. *J. Geophys.*
473 *Res.* **112**, B08306 (2007).
- 474

475 **Figure captions**

476 **Figure 1** Tectonic map in and around the Bungo Channel, southwest Japan. The thin
477 black lines represent isodepth contours of the upper surface of the Philippine
478 Sea plate subducting from the Nankai Trough, represented by the thick barbed
479 black line. The 10 km, 20-50 km, and > 60 km contour lines are taken from
480 Baba et al. (2002)¹⁷, Hirose et al. (2008)¹², and Nakajima and Hasegawa
481 (2007)¹⁸, respectively. The arrows indicate the plate motion velocity vector of
482 the Philippine Sea plate with respect to the Amurian plate estimated by
483 DeMets et al. (2010)¹. The light-blue solid circle denotes the approximate
484 location where the Bungo Channel slow slip events took place. The red solid
485 circles and blue solid squares denote the GNSS stations used for the inversion
486 analysis in this study and reference stations to calculate the common-mode
487 error, respectively. The grey squared area is the study region in the map of the
488 Japanese islands.

489
490 **Figure 2** Spatial distribution of horizontal displacement fields associated with the
491 Bungo Channel L-SSE at each 0.1-year time step during the period from
492 2018.0 to 2020.0. The red and blue arrows indicate the observed
493 displacements and the calculated displacements obtained from the
494 spatiotemporal slip distributions shown in Fig. 4, respectively. (a) 2018.0-
495 2018.1. The scale of 0.5 cm for the arrow is shown. (b) 2018.1-2018.2. (c)
496 2018.2-2018.3. (d) 2018.3-2018.4. (e) 2018.4-2018.5. (f) 2018.5-2018.6. (g)
497 2018.6-2018.7. (h) 2018.7- 2018.8. (i) 2018.8-2018.9. (j) 2018.9-2019.0. (k)
498 2019.0-2019.1. (l) 2019.1-2019.2. (m) 2019.2-1019.3. (n) 2019.3-2019.4. (o)

499 2019.4-2019.5. (p) 2019.5-2019.6. (q) 2019.6-2019.7. (r) 2019.7-2019.8. (s)
500 2019.8-2019.9. (t) 2019.9-2020.0.

501

502 **Figure 3** Same as Fig. 2 except for vertical displacement fields. The red and blue bars
503 indicate the observed and calculated displacements obtained from the
504 spatiotemporal slip distributions shown in Fig. 4, respectively. If the bars are
505 above and below the black horizontal bars, which represent locations of the
506 GNSS stations, they indicate uplift and subsidence, respectively. The scale of
507 0.5 cm for the bar is shown in (a).

508

509 **Figure 4** Slip distributions of the Bungo Channel L-SSE for the 0.1-year time step
510 during the period from 2018.0 to 2020.0. The arrows indicate the directions
511 and amounts of the slip, and the circles at the tips of the arrows indicate the
512 estimation errors of 1σ . The contour lines with yellowish colour show the
513 amounts of slip with an interval of 1 cm. Areas with a resolution of less than
514 0.15 are masked in grey. The light blue dots indicate the epicentres of tectonic
515 tremors that occurred during each period. (a) 2018.0-2018.1. (b) 2018.1-
516 2018.2. (c) 2018.2-2018.3. (d) 2018.3-2018.4. (e) 2018.4-2018.5. (f) 2018.5-
517 2018.6. (g) 2018.6-2018.7. (h) 2018.7- 2018.8. (i) 2018.8-2018.9. (j) 2018.9-
518 2019.0. (k) 2019.0-2019.1. (l) 2019.1-2019.2. (m) 2019.2-1019.3. (n) 2019.3-
519 2019.4. (o) 2019.4-2019.5. (p) 2019.5-2019.6. (q) 2019.6-2019.7. (r) 2019.7-
520 2019.8. (s) 2019.8-2019.9. (t) 2019.9-2020.0.

521

Figures

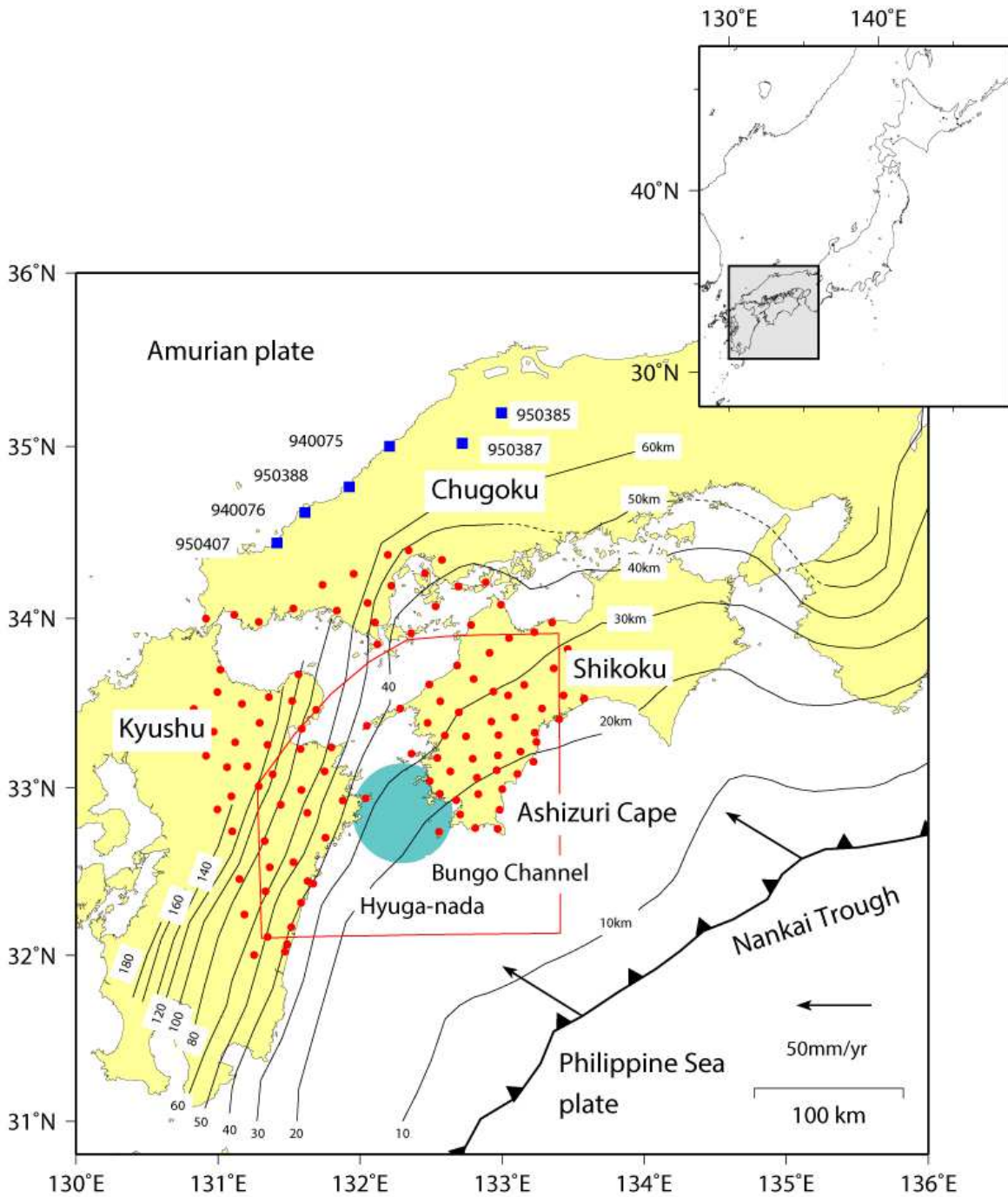


Figure 1

Tectonic map in and around the Bungo Channel, southwest Japan. The thin black lines represent isodepth contours of the upper surface of the Philippine Sea plate subducting from the Nankai Trough, represented by the thick barbed black line. The 10 km, 20-50 km, and > 60 km contour lines are taken

from Baba et al. (2002)¹⁷, Hirose et al. (2008)¹², and Nakajima and Hasegawa (2007)¹⁸, respectively. The arrows indicate the plate motion velocity vector of the Philippine Sea plate with respect to the Amurian plate estimated by DeMets et al. (2010)¹. The light-blue solid circle denotes the approximate location where the Bungo Channel slow slip events took place. The red solid circles and blue solid squares denote the GNSS stations used for the inversion analysis in this study and reference stations to calculate the common-mode error, respectively. The grey squared area is the study region in the map of the Japanese islands.

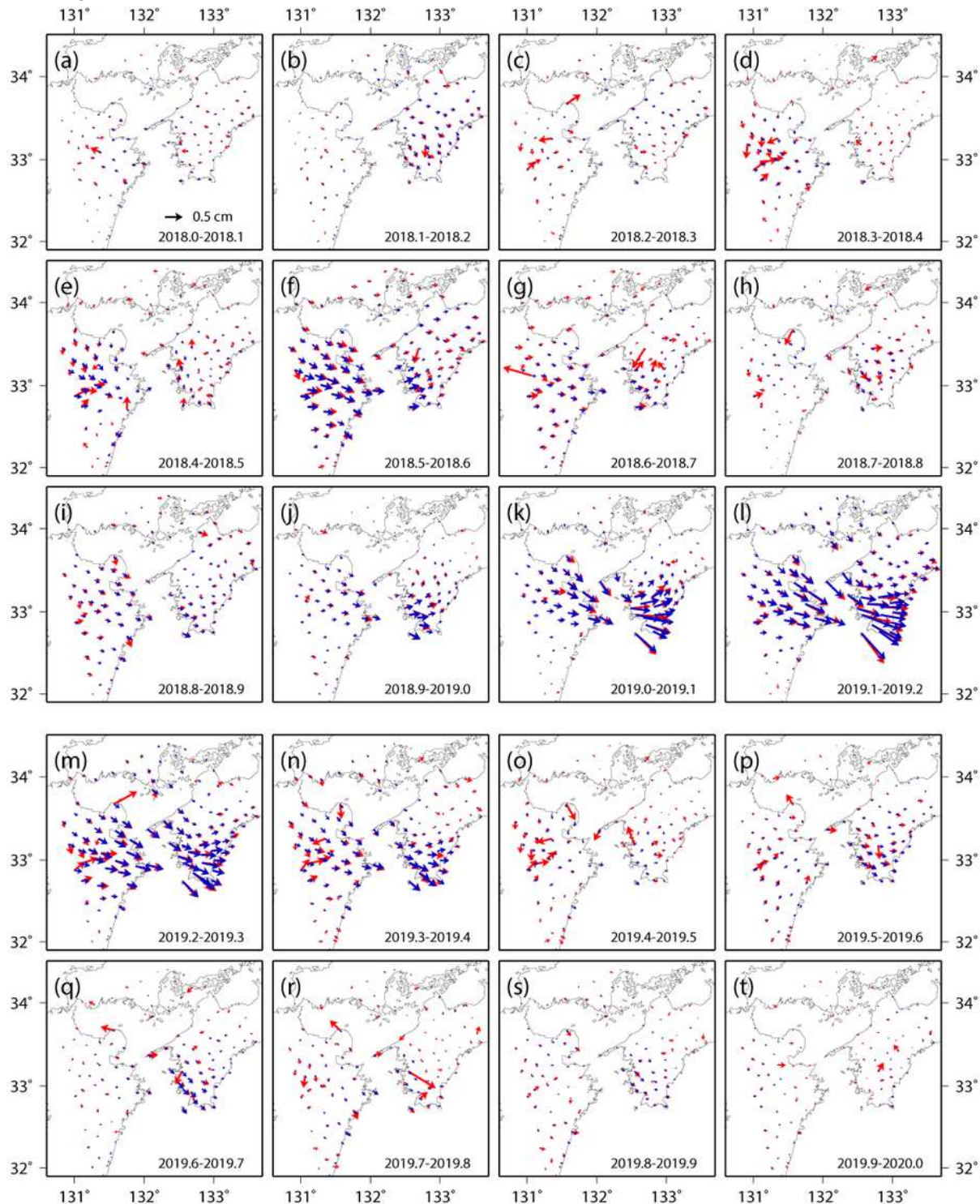


Figure 2

Spatial distribution of horizontal displacement fields associated with the Bungo Channel L-SSE at each 0.1-year time step during the period from 2018.0 to 2020.0. The red and blue arrows indicate the observed displacements and the calculated displacements obtained from the spatiotemporal slip distributions shown in Fig. 4, respectively. (a) 2018.0-2018.1. The scale of 0.5 cm for the arrow is shown. (b) 2018.1-2018.2. (c) 2018.2-2018.3. (d) 2018.3-2018.4. (e) 2018.4-2018.5. (f) 2018.5-2018.6. (g) 2018.6-2018.7. (h) 2018.7-2018.8. (i) 2018.8-2018.9. (j) 2018.9-2019.0. (k) 2019.0-2019.1. (l) 2019.1-2019.2. (m) 2019.2-2019.3. (n) 2019.3-2019.4. (o) 2019.4-2019.5. (p) 2019.5-2019.6. (q) 2019.6-2019.7. (r) 2019.7-2019.8. (s) 2019.8-2019.9. (t) 2019.9-2020.0.

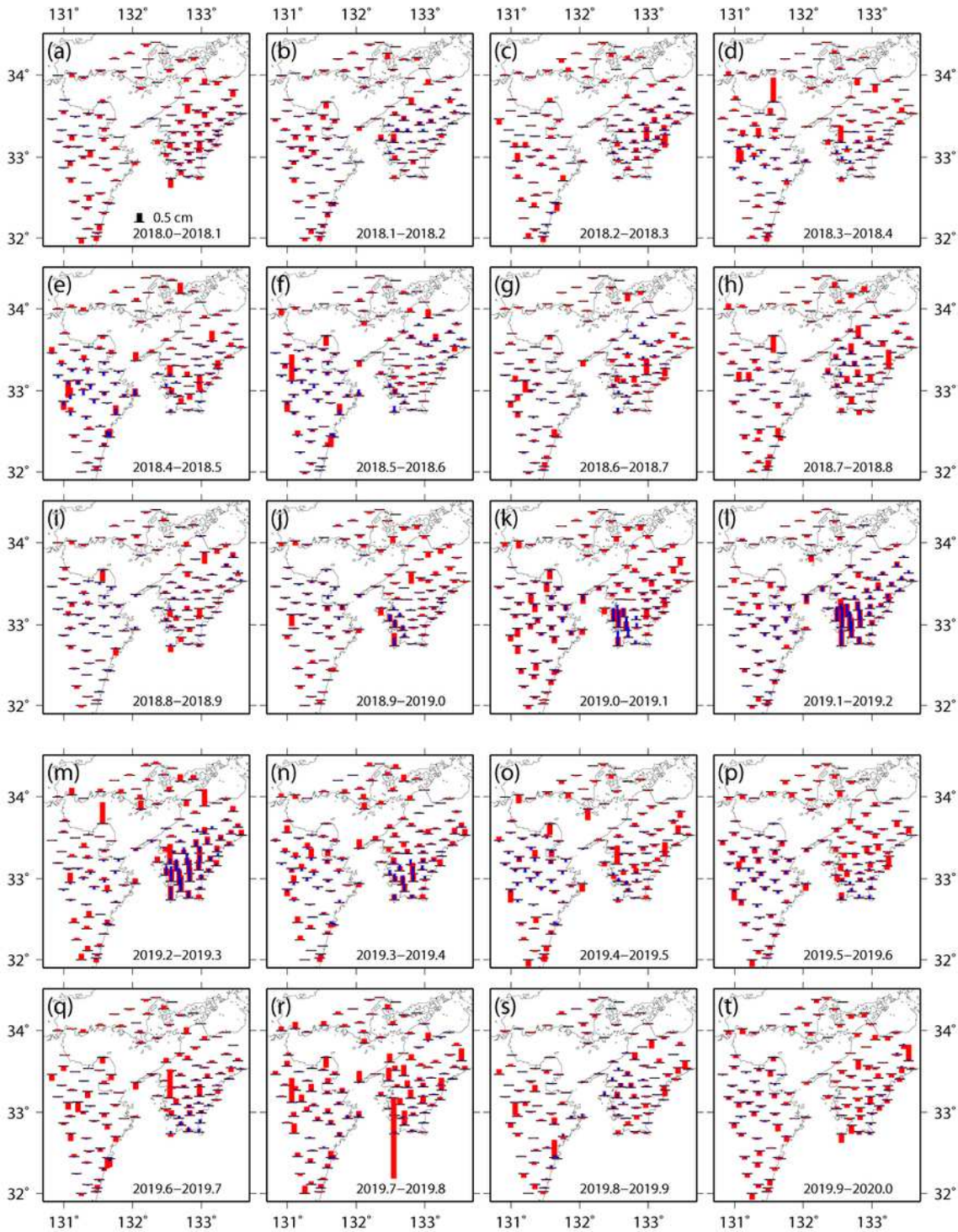


Figure 3

Same as Fig. 2 except for vertical displacement fields. The red and blue bars indicate the observed and calculated displacements obtained from the spatiotemporal slip distributions shown in Fig. 4, respectively. If the bars are above and below the black horizontal bars, which represent locations of the GNSS stations, they indicate uplift and subsidence, respectively. The scale of 0.5 cm for the bar is shown in (a).

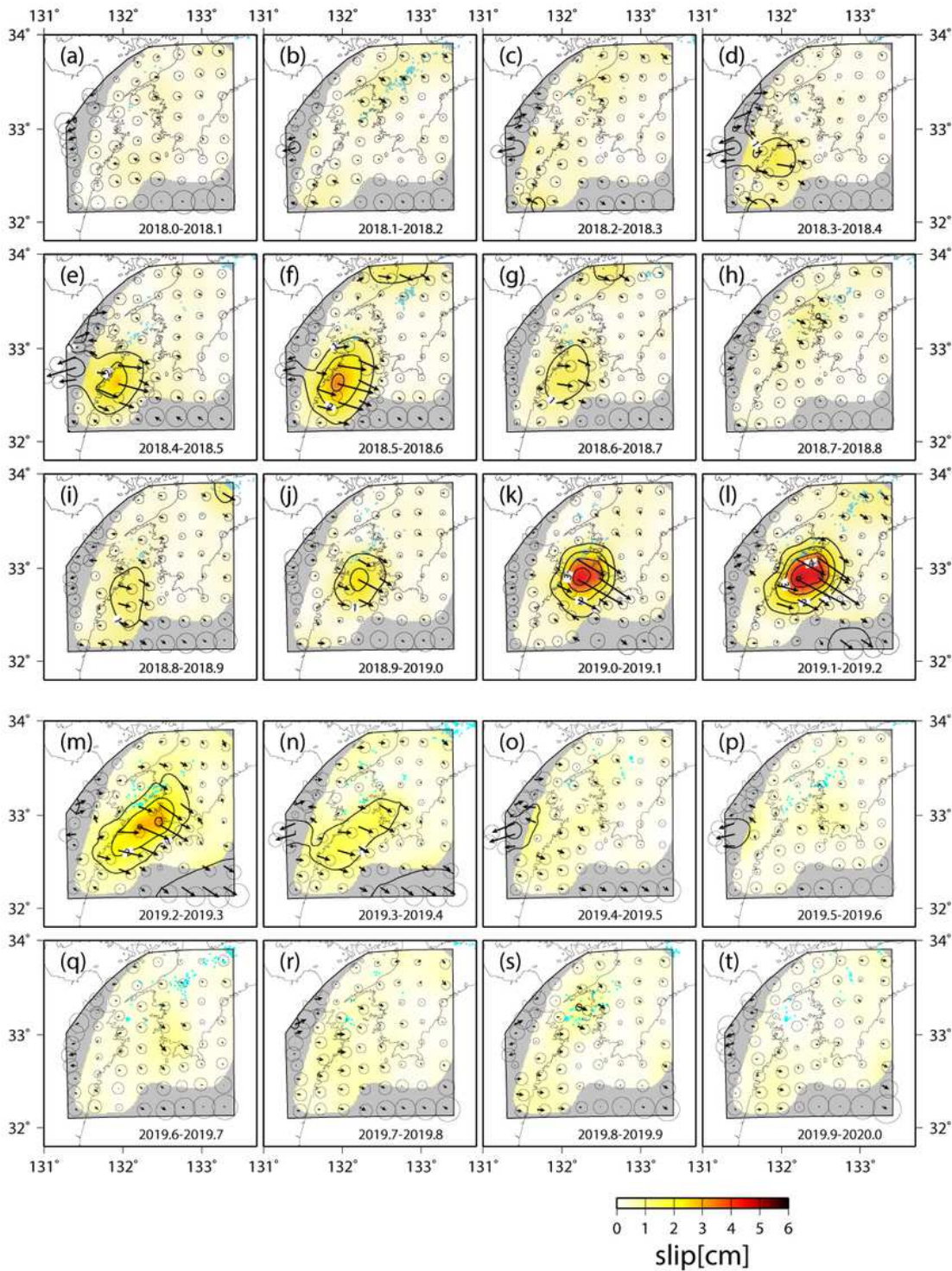


Figure 4

Slip distributions of the Bungo Channel L-SSE for the 0.1-year time step during the period from 2018.0 to 2020.0. The arrows indicate the directions and amounts of the slip, and the circles at the tips of the arrows indicate the estimation errors of 1σ . The contour lines with yellowish colour show the amounts of slip with an interval of 1 cm. Areas with a resolution of less than 0.15 are masked in grey. The light blue dots indicate the epicentres of tectonic tremors that occurred during each period. (a) 2018.0-2018.1. (b)

2018.1-2018.2. (c) 2018.2-2018.3. (d) 2018.3-2018.4. (e) 2018.4-2018.5. (f) 2018.5-2018.6. (g) 2018.6-2018.7. (h) 2018.7-2018.8. (i) 2018.8-2018.9. (j) 2018.9-2019.0. (k) 2019.0-2019.1. (l) 2019.1-2019.2. (m) 2019.2-2019.3. (n) 2019.3-2019.4. (o) 2019.4-2019.5. (p) 2019.5-2019.6. (q) 2019.6-2019.7. (r) 2019.7-2019.8. (s) 2019.8-2019.9. (t) 2019.9-2020.0.

Supplementary Files

This is a list of supplementary files associated with this preprint. Click to download.

- [Supportinginformation.docx](#)